Energy balance analyses during Standard Penetration Tests in a Virtual Calibration Chamber

Ningning Zhang[a,b,*]; Marcos Arroyo[a]; Matteo Oryem Ciantia[c]; Antonio Gens[a]

[a] *Department of Geotechnical Engineering and Geosciences, Polytechnic University of Catalonia (UPC), SPAIN*

[b] *Institute of Geotechnical Engineering, RWTH Aachen University, Germany*

[c] *School of Science and Engineering, University of Dundee, UK*

*Corresponding author at: Department of Geotechnical Engineering and Geosciences, Polytechnic University of Catalonia (UPC), SPAIN. E-mail address: ningning.zhang@upc.edu (N. Zhang)

ABSTRACT

The Standard Penetration Test (SPT) is the most popular example of dynamic probing, a large category of soil testing techniques. Understanding and interpretation of these tests is hampered by the difficulties of reproducing them under controlled laboratory conditions. The virtual calibration chamber technique, based on the Discrete Element Method (DEM), may supplement or substitute this complex experimentation. In this paper SPT in sand are analyzed considering the energy transfer involved. Energy balances are written for the penetrating rod and for the material in the chamber. All the terms are computed for a number of cases in which the main variables controlling test response in the field - initial density and stress level- are systematically varied. The analysis confirms previous field observations indicating that, when an energy-based interpretation is used, SPT provides a value of equivalent penetration resistance that is the same that would be obtained with a static cone penetration test. The analyses also provide an unequivocal explanation for this observation: although the impacting rod shows complicated dynamics the response of the sand is quasi-static.

KEYWORDS: standard penetration test; energy; calibration chamber; discrete element method

MANUSCRIPT submitted to *Computers and Geotechnics*

Authors: N. Zhang et al.

1 Introduction

The dynamic probing technique, in which a tool is driven into the soil by striking it with a hammer blow is employed for geotechnical site investigation in a variety of devices, from the large Becker Penetration Test (BPT) to hand-held light dynamic penetrometers such as the Panda. Dynamic probing is also characteristic of the Standard Penetration Test (SPT), in which a sampler positioned on the end of a boring rod is driven into the soil from the bottom of a borehole. In the SPT the blows required to drive the sampler 300 mm after an initial advance of 150 mm are counted as *N*. SPT results are widely used in geotechnical engineering as a basis to estimate soil properties (Schnaid, 2008), to design foundations (Burland & Burbridge, 1983) or evaluate liquefaction potential (Idriss & Boulanger, 2008).

Despite the SPT being a very frequently used in-situ test its results are not very highly rated (e.g. Robertson, 2012). The SPT is thought of as unreliable and unlikely to guarantee consistency in derived soil properties and parameters. This limitation stems from two important reasons:

(a) It is difficult to control the test precisely and guarantee repeatability of results;

(b) Test interpretation is overly reliant in empirical methods, typically burdened with a very restricted range of application and large associated uncertainties.

To address these shortcomings one of the more fruitful avenues of research has relied on the development of energy-based approaches. Energy-based normalizations of the reported *N*-value are now widely recognized as key to improve SPT test execution repeatability (e.g. Reading et al. 2010). After developing systems to record the energy input from hammer blows on the rod-sampler system, Schmertmann & Palacios (1979) introduced an energy normalized blow number, N_{60}, which was later identified as the best means to compare SPT results obtained using different systems (Seed et al., 1985; Skempton, 1986). Test execution standards (e.g. CEN ISO 22476-3, British Standards -2005) now systematically require evaluation of N_{60}.

Going beyond input normalization, energetic considerations have also been used to open new ways of interpreting SPT results (Hettiarachchi & Brown, 2009; Schnaid et al., 2009) by establishing an energy balance of the soil-sampler interaction. In particular, Schnaid et al., (2009) defined a work-based equivalent dynamic penetration resistance, $q_{dE,}$ and equating it to the result of conventional bearing capacity formulas obtained good agreement with reference empirical results for sands (Hatanaka & Uchida, 1996; Liao & Whitman, 1985). The fact that static bearing capacity formulas were succesfully applied to interpret SPT results in granular soils suggests that the work-corrected dynamic penetration resistance q_{dE} cannot be very different from static penetration resistance, q_t, as measured by the CPTu. Schnaid et al., (2017) went on to compare both measurements and obtained very good agreement.

This result has implications for the longstanding problem of obtaining reliable SPT-CPT correlations. Such correlations are key, for instance, to interpret the historical record of failures (e.g. Olson & Stark, 2002), but also to make better use of limited site investigation budgets -when only one of the two tests may be available at a particular location (Lingwada et al. 2015). These correlations typically relate the ratio q_c/N_{60} with physical characteristics of soils, such as mean grain size D_{50}, (Robertson et al., 1983), fines content (Chin et al. 1988) or soil behavior type (SBT, Lunne et al. 1997). They typically show large dispersion, even when the input-energy normalized N_{60} is employed. At the root of such dispersion is the complex dependency of work dissipation during dynamic probing on different soil characteristics (Jefferies & Davies, 1993).

To gain understanding of this issue numerical simulation using the discrete element method (DEM) can be helpful. DEM is advantageous to deal with dynamic problems of soil-tool interaction in granular materials, as it can give simultaneously very precise information about macroscale observables and access to underlying microscale mechanisms (Butlanska et al. 2014, Ciantia et al. 2019b).

The potential of DEM for energy analysis is also well demonstrated. For instance, Hanley et al., (2017) tracked all decomposed energy components in the simulation of triaxial compression of large-scale, polydisperse numerical samples sheared to critical state. They concluded that frictional dissipation was almost equal to work input at the boundary independently of initial sample density. In the simulation of a medium-velocity (e.g. 5 m/s) impactor penetration in sand, Holmen et al., (2017) identified the distribution of frictional sliding energy (particle-particle and particle-intruder) and energy terms of the impactor. They concluded, again, that most of the energy in the system was dissipated by friction, to which particle fracture may contribute. Zhang & Evans (2019) simulated a higher-velocity impact (25-40 m/s) – free falling torpedo anchor installation. In their study, a relatively larger ratio of collisional energy to frictional energy dissipation was obtained, due to the fast impact. All the prior studies have encouraged the potential of exploring the energy transfer mechanisms in SPT.

The authors have recently shown (Zhang et al. 2019) that 3D DEM models are able to simulate SPT in granular soils. In that work key macroscopic test results such as the relation between SPT blowcount and density and confinement were correctly reproduced. Energy blow input normalization was also proven to work correctly in the models. This previous work is here extended, describing and illustrating the performance of the necessary numerical tools to analyze energy balances and track dissipation within the granular soil during dynamic probing experiments in virtual calibration chambers.

In the following sections, we first describe the numerical testing system used for the simulations. We then describe the different energy components relevant for the problem, present the relevant energy balance equations and track energy component evolution during a representative test. Results from a suite of dynamic tests under different initial soil conditions are then examined, both at the macroscale and the microscale. The Schnaid et al., (2009) equivalence between energy-corrected dynamic penetration and static penetration is then examined. All the numerical models described in this work were built using the DEM code PFC3D (Itasca Consulting Group, 2016).

2 A virtual calibration chamber for the standard penetration test

The development and validation of a DEM-based virtual calibration chamber (VCC) for the SPT is detailed in Zhang et al. (2019). In what follows we briefly recall the essential aspects of the model set up for ease of reference.

2.1 Fontainebleau sand analogue

To increase the engineering relevance of the study the discrete element properties were selected to mimic the mechanical responses of a physical sand. A discrete analogue of Fontainebleau sand, a fine silica sand extensively used in geotechnical research, was thus created using unbreakable spherical particles. *Particle rotation was prohibited in order to roughly mimic the effect of non-spherical particle shapes. This approach, which can be traced back to Ting et al. (1989), has been successfully applied in previous work with angular granular materials (Arroyo et al., 2011; Calvetti et al., 2015; Ciantia et al., 2016) where, as here, the focus was on macroscopic response. A more realistic approach to particle shape representation may be based on image-calibrated moment-rotation contact laws, as recently illustrated by Rorato et al (2020a, 2020b). In this exploratory study of energy balances in VCC this refinement was left aside, as were other important particle-scale features, like crushability (Ciantia et al., 2015), or surface roughness effects (Otsubo et al., 2017).*

Contacts between particles are elasto-plastic. Slip behavior at contacts is limited by a friction coefficient μ. A simplified Hertz–Mindlin contact model is used to represent non-linear contact stiffness. In this model, the elastic properties of the material grains, i.e. shear modulus, G, and Poisson's ratio υ, control contact stiffness.

Macroscopic (i.e. specimen scale) calibration of DEM such as that performed here is a well-established practice in DEM simulation (Coetzee, 2017). This was also the approach followed here and the contact model properties (G, μ, v) (Table 1) were taken from a calibration presented by Ciantia et al., (2019a). The original calibration was carried out simulating two triaxial compression tests at low confining pressure (100 kPa) as reported by Seif El Dine et al. (2010). Since in this study a new version of the PFC software was employed, the triaxial calibration set was simulated again. The numerical tests were performed using a cubical cell of 4 mm in size containing 11,000 elements. Element sizes for this cubical cell were selected to closely match the PSD of Fontainebleau sand (Figure 1), with diameters ranging from 0.1 to 0.4 mm. The match obtained between the numerical model responses and the physical macroscopic responses with the new code was deemed satisfactory (Figure 2).

2.2 Model construction

The construction of a 3-dimensional virtual calibration chamber to execute SPT (Figure 3) followed a procedure described by Arroyo et al., (2011). Table 2 lists the geometrical features of the virtual calibration chamber. A scaling factor of 79 was applied to upscale the particle sizes to obtain a manageable number of particles. A rod/particle ratio, n_p = 3.06, was thus obtained, similar to that employed in previous studies (Arroyo et al., 2011; Ciantia et al., 2016). All the chamber boundaries are frictionless.

Specimens were created to specified relative density using the radius expansion method (REM). Isotropic compression to 5 kPa in which inter-particle friction was reduced was used to attain the target porosity. After equilibration, inter-particle friction was reset to the calibrated value and isotropic stress was ramped up to the target level. In all the simulations, a local damping of 0.05 (Cundall, 1987) was employed and no viscous damping was considered.

A closed ended rod is a feature of some dynamic probing tests, like the BPT, and may be also interpreted as representing a plugged SPT sampler. Sampler plugging in sand has been assumed in previous SPT interpretation methods (Schnaid et al., 2009). Hereto a flat-ended rod was created using a rigid closed-ended cylinder to mimic a plugged SPT sampling tube. By default the rod surface was set to be frictional, although the effect of this setting was addressed in some specific simulations (see below). *The rod is assumed to be of steel material and with a length of 10 m.*

The rod was firstly driven into the sample at a constant rate of 40 cm/s until a depth of 15 cm was attained. *Butlanska et al. (2010) showed that rates between 2 and 50 cm/s did not change the static penetration resistance observed in a VCC. The initial driving rate led to an inertial number < 0.01 indicating that quasi-static conditions could be maintained during the constant penetration (Ciantia et al., 2019b; Khosravi et al., 2020).* A slight pull-back of the rod was performed before launching dynamic penetration, to avoid locked-in forces. During that process, the rod was pulled up and pushed down alternatively with progressively reduced magnitudes of velocity in order to lower the tip resistance to 0.

During rod penetration, the VCC radial boundary was maintained at constant radial stress using a servo-mechanism. The same stress level was also maintained at the top horizontal boundary. On the other hand, the bottom horizontal boundary was fixed and no displacement was allowed.

2.3 SPT simulations

Dynamic driving was achieved by imposing on the rigid rod a pre-specified input force-time evolution. The time-dependent input force (Figure 4) was derived using a model proposed by Fairhurst (1961) to approximately represent the input force characteristics of an SPT hammer blow (63.5 kg weight and 0.76 m falling distance). *To avoid bottom boundary effects, the value of equivalent blow counts N is computed as the ratio of the 30 cm reference distance to the single-blow penetration depth $\Delta\rho$.*

The main soil state variables affecting dynamic penetration results are density and stress level. These are represented here by relative density D_r and mean confining pressure P_0. Results from 12 specimens are presented here. They combine four density levels, namely very dense (D_r =82%), dense (D_r =72%), medium (D_r =60.5%) and loose (D_r =38.6%) and three confining stress levels (P_0 =100 kPa, 200 kPa and 400 kPa). Relative density levels were computed assuming that maximum and minimum void ratios of Fontainebleau (e_{min} = 0.51; e_{max} = 0.9) were also valid for its discrete analogue. Impact tests were conducted in all the 12 specimens using always the above described force-time signal. The main characteristics of these DEM-based tests are collected in Table 3.

3 Energy components in the system

Dynamic rod penetration into sand is a dissipative process in which the granular assembly transits in between two equilibrium states (from the at-rest position before hammer release -at time $t = 0$- to the at-rest position after penetration ends -at time $t = t_{eq}$). During this process energy exchanges and dissipation take place in the system. All relevant energy terms were traced during each simulation. The variables encountered in energy calculations were expressed on a coordinate system oriented like that illustrated in Figure 3 but with origin located at the center of the chamber bottom wall.

For subsequent analyses, it is useful to consider separately two subsystems: the driven rod and the soil in the calibration chamber.

3.1 Work and energy components for the rod subsystem

The rod is assumed rigid and, therefore, energy delivered by the hammer impact on the rod top, W_H can be theoretically computed by integrating the impact force F_{drv} multiplied by *the simulated* rod velocity history v_r

$$W_H = \int_0^{t\_eq} F_{drv}(t) v_r(t) dt \qquad (1)$$

Where $t_{\_eq}$ is the time for equilibration.

Following the reasoning presented by Odebrecht et al., (2005), we also considered the work done by the rod self-weight during rod displacement, i.e. the change in potential energy of the rod, ΔU_R. It can be computed by integrating the rod gravitational forces $m_r g$ multiplied by the rod velocity

$$\Delta U_R = m_r g \int_0^{t\_eq} v_r(t) dt \qquad (2)$$

As rod driving proceeds, the soil in the chamber resists the rod advance. The work done by the soil resisting rod driving R_R can be calculated by integrating the recorded reaction force from the particles F_{rea} times the rod velocity.

$$R_R = \int_0^{t\_eq} F_{rea}(t) v_r(t) dt \qquad (3)$$

Finally, the instantaneous kinetic energy of the rod is evaluated from the assigned value of rod mass m_r and computed rod velocity,

$$K_R = 0.5 * m_r v_r^2(t) \qquad (4)$$

3.2 Work and energy components for the VCC subsystem

3.2.1 Work done at chamber outer boundaries

In the VCC here employed top and radial boundaries of the calibration chamber are servo controlled to maintain a constant stress level during the blow, whereas the bottom boundary remains fixed. At the moving boundaries there are work fluxes that need to be accounted for. The work done at these boundaries is here denoted as W_{rad} and W_{top} respectively. Work done at each boundary is calculated by integrating the force applied on each boundary times the velocity of the boundary.

$$W_{rad} = \int_0^{t\_eq} F_{rad}(t) v_{rad}(t) dt \qquad (5)$$

$$W_{top} = \int_0^{t\_eq} F_{top}(t) v_{top}(t) dt \qquad (6)$$

Where, F_{rad} and F_{top} are the forces of radial and top boundary, respectively; v_{rad} and v_{top} are the velocities of radial and top boundary, respectively.

Another chamber boundary is given by the rod itself. The work done by the rod W_R into the chamber can be calculated by adding up the contact forces at the rod to obtain F_{act} and multiplying this resultant by rod velocity v_r,

$$W_R = \int_0^{t\_eq} F_{act}(t) v_r(t) dt \qquad (7)$$

Clearly, the forces F_{act} and F_{rea} have the same magnitude but are in opposite direction, that is $F_{act} = -F_{rea}$ and therefore the work done by the rod into the chamber is equal and opposite to the resisting work done by the soil on the rod $W_R = -R_R$.

3.2.2 Energy components within the chamber

The net energy flow into the chamber is partly dissipated and partly stored into reversible mechanisms (kinetic particle energy and strain energy at the contacts). All the relevant terms may be computed form a particle-scale perspective.

The kinetic energy of all particles E_K may be computed taking into account translational and rotational velocities of each particle *j*.

$$E_{Kt} = \frac{1}{2}\sum_{j=1}^{n_p} m_j v_j^2 \tag{8}$$

$$E_{Kr} = \frac{1}{2}\sum_{j=1}^{n_p} I_j \omega_j^2 \tag{9}$$

Where, n_p is the total number of particles, m_j, v_j, I_j and ω_j are, the mass, translational speed, moment of inertia and rotational speed of a spherical particle *j*, respectively. Note that the second term is zero in simulations such as those presented here, in which particle rotational motion is impeded.

The strain energy stored at all contacts upon particle deformation is derived from normal and shear components, termed as E_{Sn} and E_{St}, respectively,

$$E_S = E_{Sn} + E_{St} \tag{10}$$

Assuming a Hertz-Mindlin contact model, the normal component of strain energy E_{Sn} stored at all contacts is (Itasca Consulting Group, 2016):

$$E_{Sn} = \sum_{i=1}^{n_c}\left(\frac{2}{5}\left|\mathbf{F_{n\_i}}\right|\alpha_{n\_i}\right) \tag{11}$$

Where, n_c is the total number of contacts, $\mathbf{F_{n\_k}}$ is the normal force at contact *i* and α_{n_i} is the interparticle overlap at contact *i*.

The tangential component of strain energy is calculated as

$$E_{St} = \int_0^t \sum_{i=1}^{n_c} \mathbf{F_{t\_i}}\left(t\right)\frac{\Delta\dot{\mathbf{F}}_{\mathbf{t\_i}}(t)}{k_{t\_i}}dt \tag{12}$$

Where, $\mathbf{F_{t\_i}}$ is the tangential force, $\mathbf{\Delta F_{t\_i}}$ is the increment rate of tangential force and k_{t_i} is the tangential stiffness.

Before launching a dynamic test, strain energy is already present in the chamber to a certain extent. The increment of strain energy between final and initial equilibrated states is expressed as

$$\Delta E_S = E_S^{t\_eq} - E_S^0 \tag{13}$$

Where, $E_S^{t\_eq}$ is the strain energy at final state and E_S^0 is the strain energy right before launching dynamic test.

Frictional dissipation is the main mechanism for energy dissipation. A slip criterion is imposed to determine the limit of the tangential force $\mathbf{F_t}$, as described

$$\mathbf{F_t} > \mu \mathbf{F_n} \tag{14}$$

Where, μ is the friction coefficient.

When friction slip occurs between contacts, the energy dissipated by frictional sliding D_F over all contacts can be also calculated

$$D_F = \int_0^{t\_eq} \sum_{i=1}^{n_c} \mathbf{F_{t\_i}}(t) \Delta \dot{\mathbf{U}}_\mathbf{i}(t) dt \tag{15}$$

Where, $\Delta \dot{\mathbf{U}}_\mathbf{i}$ is the increment rate of slip displacement.

Besides frictional sliding, energy can also be dissipated by numerical damping, which is denoted here as D_D and calculated as

$$D_D = \int_0^{t\_eq} \sum_{i=1}^{n_c} \mathbf{F^d}(t)(\dot{\mathbf{x}}(t)) dt \tag{16}$$

Where, $\mathbf{F^d}$ is the damping force and $\dot{\mathbf{x}}$ is the relative translational velocity.

Generally speaking, damping is introduced in mechanical models to represent indirectly small energy sinks that are too onerous to be directly modelled (Crandall, 1970). DEM based simulations are no exception and damping is used, for instance, to represent heat radiation. As a result of damping elastic fixed-fabric oscillations are avoided and equilibrium is achieved in reasonable time. The damping ratio is set here as a relatively small value 0.05. It is shown below that the energy dissipation due to this term is pretty small and has a small influence on the energy balance. Of the above-mentioned components W_R, W_{rad}, W_{top}, E_K and ΔE_S, might have either positive or negative values, while D_F and D_D are positive for any loading step.

4 Energy balance analyses during SPT blows

4.1 Energy balance of driven rod

By considering all the above-identified energy components, the energy balance equation for the rod subsystem can be written, at any time t, as

$$W_H + R_R = K_R - \Delta U_R \quad (17)$$

Test Loose_200 is selected as the main illustrative example in this section; some relevant results for all tests are collected in Table 4. The evolution of the variables entering the rod energy balance, such as driving force F_{drv}, penetration velocity v_r, reaction force on rod F_{rea} and rod displacement $\Delta\rho$ with time are illustrated in Figure 5. The records are displayed until the variables reach stationary values (that is at t = 0.1 s for all the variables except for the driving force, which is represented in a shorter timescale as it is zero after 0.02 s). The driving force presents a shape of successive pulses of progressively reduced intensity and terminates at time 0.004s (Figure 5a). The rod attains a maximum value of velocity 1.4m/s (Figure 5b). The reaction force on rod is composed by forces acting on the tip and the shaft. Its trend (Figure 5c) appears very similar to the tip resistance curve (see below, Figure 13a). In this blow the rod was driven to a permanent penetration of 0.026 m (Figure 5d).

Based on the recorded signals shown in Figure 5, the evolution of each energy term on the rod can be computed. In Figure 6, the results are plotted for two tests, (Loose_200 and Very dense_200) at the extremes of initial density. In both tests the hammer work input reaches a final constant value when the impact terminates, corresponding to the separation point between the hammer and the rod. The hammer work input results in different rod behavior for the loose and very dense cases.

In the loose case (Figure 6a) the rod kinetic energy has a sharp increase until attaining its peak value and then follows a sharp decrease until the rod stops. The contribution of rod potential energy (41.4 J) to the energy balance is significant, approximately 25% of the hammer input energy in this loose case. In the very dense case (Figure 6b) the rod rebounds: the final contribution of the potential energy term is a small negative value (-7.5 J). The hammer energy input is rapid, while K_R and R_R last longer, until penetration is finished and travel almost in parallel, indicating an almost instant transform between the rod kinetic energy and the resistant work. With the input force-time history prescribed for the hammer, the energy finally delivered to the sample (sum of the final values of hammer input energy and the rod potential energy change) is 46.7 % of the hammer free fall potential energy for the loose case and 42.1 % for the very dense case. These values correspond to the input energy ratios, *ER* (Table 4) that are used to normalize blowcounts (*N*) and obtain N_{60}. Energy ratios observed in the field also decrease as the soil gets denser (Odebrecht et al. 2005).

To confirm that all the sources of energy on rod were correctly identified and that the calculations of each term are correct, the energy balance error ΔW was tracked during the simulation as

$$\Delta W = W_H + U_R + R_R - K_R \quad (18)$$

Figure 7 shows the evolution of energy balance error ΔW normalized by the rod resistance term R_R. The energy balance error is very small, confirming that the expressions for each energy term on rod are correctly evaluated and the energy balance is consistent.

4.2 Energy balance of the chamber

Using the previously defined components, the balance of energy for the calibration chamber subsystem may be written as:

$$W_R + W_{rad} + W_{top} = D_F + D_D + E_K + \Delta E_S \quad (19)$$

Energy balance computations in the VCC are also explored using the Loose_200 test as main guidance; Table 5 includes some key results for all the different specimens.

Figure 8 represents the time evolution of the main work components for a loose and very dense case. Damping energy and translational kinetic energy (Eq. 8) are so much smaller throughout than the other terms (see values in Table 5), that they are not represented in the figure to avoid clutter. It is obvious from the graph that the work input is predominantly dissipated by frictional sliding between contacts. However, the dynamics are simpler for the loose case than for the very dense case.

In the loose case (Figure 8a) there is a monotonous rise in rod work, almost exactly matched by frictional dissipation. In the very dense case (Figure 8b) the role of elastic storage at particle contacts and chamber boundary effect is more visible. The moment in which the rod starts rebounding the work it delivers to the sample (W_R) peaks and stored elastic energy at the particle contacts (ΔE_S) starts decreasing. This decrease continues until a negative value is attained. The blow has relaxed somewhat the contact network. The damping role of the servo-controlled constant-stress radial boundary is also clear: expanding (i.e. absorbing energy) while the rod advances but contracting (i.e. contributing work) when the rod rebounds.

Figure 9 shows (for the Loose_200) case the evolution in time of the variables used for calculation of work fluxes at the different granular boundaries: rod action force F_{act}, penetration velocity v_r, radial boundary force F_{rad}, radial boundary velocity v_{rad}, top boundary force F_{top} and top boundary velocity v_{top}. These records are shown up to 0.1 s when the system has reached an equilibrated state.

Rod action in the chamber (Figure 9a) is of equal magnitude and opposite sign to rod reaction force (Figure 5c). More interesting perhaps are the oscillations in the radial and top boundary wall forces and velocities resulting from the servo-control mechanism aiming for constant stress (Figure 9c to f). They present a high frequency pattern during the initial 4 ms that correspond to the rod main acceleration and deceleration cycle and then they steadily recover the target value.

Although the magnitudes of forces and velocities at the two servo-controlled boundaries (top and radial) are similarly small, the ensuing boundary displacements are not (Figure 10). The top wall displacement is negligible, but no so that of the radial wall. The radial wall displaces rapidly outwards during the blow (approximately until 0.5 ms), then hovers at around 2.5 cm outward displacement during the main rod cycle (approximately until 4 ms), finally a rapid contraction motion is observed. The radial wall final position results in an inward motion of 6 mm (Figure 10a).

Similar to Eq. 17, Eq. 19 can be written in a form of energy error

$$\Delta E = W_R + W_{rad} + W_{top} - D_F - D_D - E_K - \Delta E_S \tag{20}$$

The three work terms can be combined to give work done on the granular mass as $W = W_R + W_{rad} + W_{top}$. The other four terms can be classified into two groups: non-recoverable energy sinks (D_F and D_D) and storage terms (E_K and E_S). Figure 11 shows the evolution of error in energy balance normalized by rod work input. The ratio is negligible, confirming again the accuracy of the computations.

4.3 Tip resistance and contact forces during rod advance

Figure 12 illustrates the evolution of friction dissipation and rod work input vs dynamic penetration depth. For the loose specimen (Figure 12a) they follow almost parallel trajectories, increasing proportionally with depth during most of the process. A tiny lag between the rod work input and the friction term is present: that is mostly due to strain energy and chamber boundary terms. In the very dense specimen (Figure 12b) rod maximum advance is much smaller and is completely erased by the rebound, ending at negative values. The differences between rod work input and frictional dissipation are significant, both in advance and in retreat, due to the larger role of elastic storage and boundary work.

Figure 13a presents the dynamic penetration curve of test Loose 200, with indications of the phases *–I “acceleration”, II “deceleration”, III “unloading”*- defined by Zhang et al (2019). As a way of contrast the result for test Very Dense 200 is shown in Figure 13b. It is clear that the plastic advance of the rod (*phase II*) is not fully developed and the rebound magnitude is such that the rod tip loses contact with the granular mass.

The evolution of the contact force network during dynamic penetration (Figure 14) offers a microscale perspective on the evolution of rod-soil interactions during the blow. In the figure 3D contact force vectors are represented in planar projection along a vertical section containing the chamber axis. Forces exceeding the whole ensemble average (μ) are plotted in dark grey if CF < μ +5σ while they are in black if CF > μ +5σ where σ is the standard deviation. The forces smaller than the average force are plotted in light grey. The lines join the centroids of contacting spheres and their thickness is proportional to the magnitude of the normal force.

The observation points include not only the characteristic time points t_0, t_1, t_2, t_3 and t_4 used for distinguishing the dynamic process, but also several time points between these characteristic points such as t_{0_1}, t_{1_1}, t_{1_2} and t_{2_1} (Figure 13a).

The first snapshot corresponds to the moment just before the blow, with residual forces largely relaxed (Figure 14a) due to rod pull-back. During the whole penetration process, the magnitude of contact forces varies significantly only within a region of about 3 rod diameters around the tip. Contact forces in this area increase sharply during the short impact period from time t_0 to t_1 (Figure 14a, b). They maintain relatively constant magnitudes till t_2, while the penetration advances (Figure 14c, d and e). After t_2, the rod rebounds and the tip unloads until the CF are close to 0 at t_3, (Figure 14f, g). After t_3, some contact force recovery is observed at the final equilibrated stage to support the rod weight ((Figure 14h).

The spatial distribution of contact forces is also interesting. The plots reveal two significant common features. The first one is that the strong force network clearly focuses on the rod tip and the other one is that the force network is sparser above the tip with relatively small forces appearing in the vicinity of the shaft. The phenomenon may be related to the restriction of particle rotation by which a small number of particles around the tip are sufficient to transmit the force from the tip. The isotropic boundary condition maintains a relatively constant network at the areas away from the rod tip.

4.4 Effect of density and stress level on energy balance terms

We have already indicated above that initial density modifies the energy transfers taking place during an SPT blow. To explore this issue more systematically, we use normalized SPT blowcount N_{60} as an index to track the behavior of the different tests. As shown in Zhang et al (2019) the values obtained from the calibration chamber tests increased with stress level and relative density following well-established experimental trends (Meyerhof, 1957; Skempton, 1986; Hatanaka & Uchida, 1996).

Figure 15 represents the ratio of frictional dissipation D_F to total energy input W in the chamber. The values for the lower N_{60} values (i.e. for the looser and/or less confined specimens) remain close but below 1, as expected. However, for the denser, more confined specimens the ratio goes above 1. This is because a part of strain energy stored before launching dynamic penetration is released during the unloading rebound of the driven rod and is afterwards dissipated by frictional sliding. *This may also be expressed, using the language of Collins (2005), as a release of frozen elastic energy due to the disturbance induced by the SPT blow.*

This effect is demonstrated clearly in Figure 16, where the change in stored strain energy is plotted at two instants for each test: when attains its maximum value (label '*Max*') and at the end of the test (label

‘*End*’). The maximum change in stored strain energy is always positive and increases almost linearly with normalized blowcount; this is simply reflecting the influence of increasing coordination number - due to increased density- and of particle overlap -due to increased confinement. At the end of penetration, the change in stored strain energy is negligible except for those tests in more confined and dense specimens, where negative values are observed.

Similarly, the role played by the servo-controlled top and radial chamber walls is affected by the N_{60} values (Figure 17). The top wall contributes positive work to the specimen (i.e. moves downward) during the whole penetration process; this contribution attains higher maxima (Figure 17a) for specimens with higher N_{60} values. The outward radial wall motion during the SPT blow also increases with N_{60}, as it does the final inward displacement (Figure 17b).

5 Relating dynamic and static penetration resistance

5.1 Frictional dissipation around the rod and shaft friction

It has been noted in this study the hammer input energy is mostly dissipated by frictional sliding between contacts regardless of sample density and stress level. It is interesting to explore the spatial distribution of that dissipation. Figure 18 shows -for Loose 200- cumulative frictional dissipation is represented in a 4 cm thick cross-section along a vertical section containing the chamber axis. Frictional dissipation takes place at contacts, but to facilitate visualization energy dissipated contributed by sliding contacts is allocated to particles, -at every contact is equally divided between the two entities involved. It can be noticed that the area where the energy is mostly dissipated by friction is highly concentrated below the rod tip and reduces rapidly when moving further away from the rod tip. There is also some dissipation along the rod shaft but with smaller magnitudes.

Rod side friction is not present in all the dynamic probing tests. For instance, in the light penetrometer Panda (Tran et al. 2019) an enlargement at the tip is designed to avoid side friction. In the SPT there is an assumption that side friction will develop in the penetrating sampler. It is therefore interesting to explore what is the effect of rod side friction on the impact dynamics. Results are illustrated in Figure 19 for the loose and very dense cases. The presence of shaft friction modifies the tip response, slightly increasing initial stiffness and reducing somewhat the peak tip reaction in the main blow. However, the main differences are those appearing during the rebound phase, which in absence of shaft friction presents high oscillations (for the loose case) or even separation and secondary impacts. The last are reminiscent of the secondary impacts at the hammer – rod interface, a well-documented observation for field SPT (Lee et al. 2010).

5.2 Equivalent penetration resistance

Schnaid et al., (2009) proposed an expression for the dynamic equivalent penetration resistance q_{dE} of SPT blows. This was proposed as a function of

$$q_{dE} = \frac{\eta_3\eta_1(hm_h g) + \eta_3\eta_1(\Delta\rho m_h g) + \eta_3\eta_2(\Delta\rho m_r g)}{\Delta\rho a} \quad (21)$$

Where $\Delta\rho$ is the permanent penetration of the sampler, h is the hammer fall height, m_h is the hammer mass, m_r is the rod mass, a is the cross-sectional area of the rod, g is the gravitational acceleration, η_1, η_2 and η_3 are, respectively, the hammer, rod and system efficiency coefficients. These coefficients are used to account for energy losses and are amenable to experimental determination (Odebrecht et al., 2005).

It is clear that the numerator in Eq. 21 expression is actually a formula calculating the delivered energy to the sampler, which is a sum of energy delivered by the hammer impact W_H and by rod self-weight U_R. These two energy terms are directly measured in the DEM simulations. Therefore the analogous version of Eq. 21 for DEM calculations can be expressed as

$$q_{dE} = \frac{W_H + U_R}{\Delta\rho a} \quad (22)$$

In the numerical tests the value of $\Delta\rho$ is taken at the moment when the rod starts the rebound and the reaction force from the ground first goes to cero. This excludes the later period of the impact in which there is not tip contact and the rod is oscillating sustained by shaft friction, as this mechanism is not present in continuous -i.e. static- penetration.

Meanwhile, a reference static tip resistance q_e may be obtained averaging the static tip resistance within the same depths as those measured during the 'deceleration' phase of dynamic probing. As illustrated in Figure 20, the equivalent dynamic penetration resistances thus computed (Table 6) are very close to the mean static tip resistances, even for high density samples. The ratio of q_{dE} / q_e is independent of soil properties.

6 Conclusions

In this study, a comprehensive study of the temporal evolution of energy transfers during SPT impacts in a 3D virtual calibration chamber filled with a sand analogue was performed. Energy balances were proposed from both the rod and the chamber subsystems, and evaluated for a series of specimens set up at varying initial conditions of density and confining stress. The main findings of this work are:

1. The Schnaid et al (2009) definition of equivalent dynamic penetration resistance for field SPT can be easily translated and applied to this numerical context.
2. The VCC results presented here confirm field observations indicating that the equivalent dynamic penetration and static cone resistances are practically coincident.
3. The kinetic energy in the soil was always negligible during the SPT blows making the inertial contributions to the mobilized strength minimal. This is the likely reason why a good correlation is obtained between the equivalent dynamic penetration resistance and the static one.
4. For specimens with N_{60} below 30 practically all the work input to the soil by the rod is dissipated by friction at the particle contacts.
5. For denser and/or more confined specimens, resulting in N_{60} values above 30 a significant rod rebound was observed, resulting on some release of initially stored elastic energy and compaction at the stress-controlled radial boundary.
6. The dynamics of the rod impact in a granular mass are significantly affected by shaft friction. A frictionless testing arrangement is likely to result in repeated impacts in dense soils.

There are some limitations in the study presented that should be noted. Some of them derive from the highly simplified material model employed. It is likely, for instance that stresses below the tip will result in particle crushing. A crushable particle model such as Ciantia et al. (2015) may be employed to explore the effect of that feature. It is also likely that the stiffness value selected for the contacts is too low and results in excessive rod rebound. For low strain problems, such as wave propagation (Otsubo et al. 2017), more refined contact models with higher initial contact stiffness give good results. These richer models should be also explored for dynamic probing in VCC in future work. Another limitation is derived from the relatively high scaling number employed which results is poor resolution of side friction development; spatially variable discretization techniques (McDowell et al. 2012) may be used to alleviate this problem. *Finally, the use of a solid rod is only a good analogy of SPT if the sampler is plugged during driving: partial plugging effects remain to be investigated.*

The dynamic boundary effects noted in the chamber were significant for the denser materials. There is some physical difficulty in implementing this kind of fast control in the laboratory –given the inertias inbuilt in the hydraulic actuators that are frequent in geotechnical practice. This may be one of the obstacles that explain the paucity of laboratory calibration chamber studies of dynamic probing. The availability of VCC models such as those presented here will surely facilitate future experimental work.

7 Acknowledgements

The first author was supported by a CSC grant. This work was partly supported by the Ministry of Science and Innovation of Spain through the research grant BIA2017-84752-R.

8 References

Arroyo, M., Butlanska, J., Gens, A., Calvetti, F., & Jamiolkowski, M. (2011). Cone penetration tests in a virtual calibration chamber. *Géotechnique*, *61*(6), 525–531. https://doi.org/10.1680/geot.9.P.067

British Standards (2005) BS EN ISO 22476-3: 2005: Geotechnical investigation and testing. Field testing. Standard penetration test

Burland, J. B., & Burbridge, M. C. (1985, December). Settlement of foundations on sand and gravel. In Institution of Civil Engineers, Proceedings, Pt 1 (Vol. 76).

Butlanska, J., Arroyo, M., Gens, A., & Sullivan, C. O. (2014). Multi-scale analysis of cone penetration test (CPT) in a virtual calibration chamber. *Canadian Geotechnical Journal*, *51*(1), 51–66. https://doi.org/dx.doi.org/10.1139/cgj-2012-0476

Butlanska, J., Arroyo, M., Gens, A., 2010. Virtual calibration chamber CPT tests on Ticino sand, in: Second Intrnational Sumposium on Cone Penetration Testing, CPT'10. Huntington Beach, California, pp. 217–224. https://doi.org/10.13140/2.1.2939.5207

Calvetti, F., Prisco, C., & Nova, R. (2015). Experimental and Numerical Analysis of Soil – Pipe Interaction. *Journal of Geotechnical and Geoenvironmental Engineering*, *130*(12), 1292–1299. https://doi.org/10.1061/(ASCE)1090-0241(2004)130

Chin C, Duann S, Kao T. SPT–CPT correlations for granular soils. In: Proceedings of the 1st international symposium on penetration testing (ISOPT-1), vol. 1; 1988. p. 335–9.

Ciantia, M. O. Arroyo, M., O'Sullivan, C., Gens, A. & Liu, T. (2019a) Grading evolution and critical state in a discrete numerical model of Fontainebleau sand, *Géotechnique.* 69(1), 1-15. https://doi.org/10.1680/jgeot.17.P.023

Ciantia, M.O., O'Sullivan, C., Jardine, (2019b). Pile penetration in crushable soils: Insights from micromechanical modelling. In: Proceedings of the XVII ECSMGE-2019 Geotechnical Engineering Foundation of the Future., pp 298-317

Ciantia, M. O., Arroyo, M., Butlanska, J., & Gens, A. (2016). DEM modelling of cone penetration tests in a double-porosity crushable granular material. *Computers and Geotechnics*, *73*, 109–127. https://doi.org/10.1016/j.compgeo.2015.12.001

Ciantia, M. O., Arroyo, M., Calvetti, F., & Gens, A. (2015). An approach to enhance efficiency of DEM modelling of soils with crushable grains. *Geótechnique*, *65*(2), 91–110. https://doi.org/[http://dx.doi.org/10.1680/geot.13.P.218

Crandall. (1970). The role of damping in vibration theory. *Journal of Sound and Vibration*, *11*(1), 3–

18.

Cundall, P. A. (1987). Distinct element models of rock and soil structure. In *Analytical and computational methods in engineering rock mechanics (ed. E. T. Brown)* (pp. 129–163). London, UK: Allen and Unwin.

Escobar, E., Benz, M., Gourvès, R., and Breul, P. (2013). "Dynamic cone penetration tests in granular media: Determination of the tip's dynamic load-penetration curve". In *AIP Conference Proceedings* (Vol. 1542, No. 1, pp. 389-392). AIP.

Fairhurst, C. (1961). "Wave Mechanics of Percussive Drilling." *Mine and Quarry Engineering* 27(4): 169–78.

Hanley, K. J., Huang, X., & O'Sullivan, C. (2017). Energy dissipation in soil samples during drained triaxial shearing. *Géotechnique*, (2011), 1–13. https://doi.org/10.1680/jgeot.16.P.317

Hatanaka, M., & Feng, L. (2006). Estimating relative density of sandy soils. *Soils and Foundations*, *46*(3), 299–313.

Hatanaka M, Uchida A. Empirical correlation between penetration resistance and internal friction angle of sandy soils. Soils Found 1996;36(4):1–9. https://doi.org/ 10.3208/sandf.36.4_1.

Hettiarachchi, H., & Brown, T. (2009). Use of SPT Blow Counts to Estimate Shear Strength Properties of Soils: Energy Balance Approach. *Journal of Geotechnical and Geoenvironmental Engineering*, *135*(6), 830–834. https://doi.org/10.1061/(ASCE)GT.1943-5606.0000016

Holmen, J. K., Olovsson, L., & Børvik, T. (2017). Discrete modeling of low-velocity penetration in sand. *Computers and Geotechnics*, *86*, 21–32. https://doi.org/10.1016/j.compgeo.2016.12.021

Idriss, I. M., & Boulanger, R. W. (2008). *Soil liquefaction during earthquakes* (Vol. 264). https://doi.org/10.1126/science.287.5454.803e

Itasca Consulting Group. (2016). PFC3D: Itasca Consulting Group, Inc. (2014) PFC — Particle Flow Code, Ver. 5.0 Minneapolis, USA.

Jefferies, M. G., & Davies, M. P. (1993). Use of CPTU to estimate equivalent SPT N 60. Geotechnical Testing Journal, 16(4), 458-468.

Khosravi, A., Martinez, A., & Dejong, J. T. (2020). Discrete element model (DEM) simulations of cone penetration test (CPT) measurements and soil classification. *Canadian Geotechnical Journal*, *57*(9), 1369–1387. https://doi.org/10.1139/cgj-2019-0512

Lee, C., Lee, J. S., An, S., & Lee, W. (2010). Effect of secondary impacts on SPT rod energy and sampler penetration. Journal of geotechnical and geoenvironmental engineering, 136(3), 522-526.

Liao, S. S. C., and Whitman, R. V. (1985). "Overburden correction factors for SPT in sand." J. Geotech.

Engrg., 112, 3, 373–377.

Lingwanda, M. I., Larsson, S., & Nyaoro, D. L. (2015). Correlations of SPT, CPT and DPL data for sandy soil in Tanzania. Geotechnical and geological engineering, 33(5), 1221-1233.

Lunne, T., Robertson, P.K., Powell, J.J.M., 1997. Cone Penetration Testing in Geotechnical Practice. Blackie Academic and Professional.

McDowell, G.R., Falagush, O., Yu, H.S., 2012. A particle refinement method for simulating DEM of cone penetration testing in granular materials. Geotech. Lett. 2, 141–147. https://doi.org/10.1680/geolett.12.00036

Meyerhof GG. Disscussion on Research on determining the density of sands by spoon penetratio testing. Proc 4th Int Conf Soil Mech Fdn Eng London 1957;3:110.

Olson, Scott M., and Timothy D. Stark. (2002) "Liquefied strength ratio from liquefaction flow failure case histories." Canadian Geotechnical Journal 39.3: 629-647

O'Sullivan, C. (2014). Advancing geomechanics using DEM. In *The International Symposium on Geomechanics from Micro to Macro (IS-Cambridge 2014)* (pp. 21–32). https://doi.org/10.1201/b17395-4

Odebrecht, E., Schnaid, F., Rocha, M. M., & de Paula Bernardes, G. (2005). Energy Efficiency for Standard Penetration Tests. *Journal of Geotechnical and Geoenvironmental Engineering*, *131*(10), 1252–1263. https://doi.org/10.1061/(ASCE)1090-0241(2005)131:10(1252)

Otsubo, M., O'Sullivan, C., Hanley, K. J., & Sim, W. W. (2017). The influence of particle surface roughness on elastic stiffness and dynamic response. *Géotechnique*, *67*(5), 452–459. https://doi.org/10.1680/jgeot.16.P.050

Reading, P., Lovell, J., Spires, K., & Powell, J. (2010). The implications of the measurement of energy ratio (Er) for the StandardPenetration Test. Ground Engineering, 43(5).

Robertson, P. K., Campanella, R. G., & Wightman, A. (1983). SPT-CPT Correlations. *Journal of Geotechnical Engineering*, *109*(11), 1449–1459. https://doi.org/https://doi.org/10.1061/(ASCE)0733-9410(1983)109:11(1449)

Robertson, P. K. (2012). The James K. Mitchell Lecture: Interpretation of in-situ tests–some insights. In Proc. 4th Int. Conf. on Geotechnical and Geophysical Site Characterization–ISC (Vol. 4, pp. 3-24).

Rorato, R., Arroyo, M., Andò, E.C.G., Gens, A. & Viggianni, G Linking shape and rotation of grains during triaxial compression of sand. Granular Matter 22, 88 (2020a). https://doi.org/10.1007/s10035-020-01058-2

Rorato, R., Arroyo, M., Gens, A., Andó, E. & Viggianni, G. (2020b) Image-based calibration of rolling resistance in discrete element models of sand, Computers & Geotechnics (accepted for publication, November 2020)

Schmertmann, J. H., & Palacios, A. (1979). Energy dynamics of SPT. *Journal of the Geotechnical Engineering Division*, *105*(GT8), 909–926.

Schnaid, F. (2008). In situ testing in geomechanics: the main tests. CRC Press.

Schnaid, F., Lourenço, D., & Odebrecht, E. (2017). Interpretation of static and dynamic penetration tests in coarse-grained soils. *Géotechnique Letters*, *7*(2), 113–118. https://doi.org/10.1680/jgele.16.00170

Schnaid, Fernando, Odebrecht, E., Rocha, M. M., & Bernardes, G. D. P. (2009). Prediction of Soil Properties from the Concepts of Energy Transfer in Dynamic Penetration Tests. *Journal of Geotechnical and Geoenvironmental Engineering*, *135*(May 2012), 1092–1100. https://doi.org/10.1061/(ASCE)GT.1943-5606.0000059

Seed, H. B., Tokimatsu, K., Harder, L. F., & Chung, R. M. (1985). Influence of SPT Procedures in Soil Liquefaction Resistance Evaluations. *Journal of Geotechnical Engineering*, *111*(12), 1425–1445. https://doi.org/10.1061/(ASCE)0733-9410(1985)111:12(1425)

Seif El Dine, B., Dupla, J. C., Frank, R., Canou, J., & Kazan, Y. (2010). Mechanical characterization of matrix coarse-grained soils with a large-sized triaxial device. *Canadian Geotechnical Journal*, *47*(4), 425–438. https://doi.org/10.1139/T09-113

Skempton, A. W. (1986). Standard penetration test procedures and the effects in sands of overburden pressure, relative density, particle size, ageing and overconsolidation. *Géotechnique*, *36*(3), 425–447.

Ting, J. M., Corkum, B. T., Kauffman, C. R., & Greco, C. (1989). Discrete numerical model for soil mechanics. *Journal of Geotechnical Engineering*, *115*(3), 769–787. https://doi.org/10.1061/(ASCE)0733-9410(1989)115

Tran, Q. A., Chevalier, B., Benz-Navarrete, M. A., Breul, P., & Gourvès, R. (2019). Numerical verification of the continuous calculation method for tip stress during the driving process of the dynamic penetration test. Soils and Foundations.

Zhang, N, & Evans, T. M. (2019). Discrete numerical simulations of torpedo anchor installation in granular soils. *Computers and Geotechnics*, *108*, 40–52. https://doi.org/10.1016/j.compgeo.2018.12.013

Zhang, N, Arroyo, M., Ciantia, M. O., Gens, A., & Butlanska, J. (2019). Standard penetration testing in a virtual calibration chamber. *Computers and Geotechnics*, *111*(3), 277–289. https://doi.org/10.1016/j.compgeo.2019.03.021

9 Tables

Table 1 DEM contact model parameters

Material	*G*: GPa	*μ*	*v*
F-Sand	9	0.28	0.2
Rod	77	0.3	0.52

Table 2 Geometrical characteristics of the virtual calibration chamber

Variable (unit)	Symbol	DEM
Chamber diameter (mm)	D_c	760
Rod outside diameter (mm)	d_c	50.8
Chamber height (mm)	H	500
Rod length (m)	l	10
Scaling factor	-	79
mean element size (mm)	D_{50}	16.6
Chamber/rod diameter ratio	D_c / d_c=R_d	15
Rod/particle ratio	d_c / D_{50}=n_p	3.06

Table 3 Basic programme of DEM-based dynamic probing tests

Test ID	D_r: %	P_0: kPa	N. of particles
Very Dense_100	82.6	100	69,166
Very Dense_200	83.0	200	69,166
Very Dense_400	83.7	400	69,166
Dense_100	74.0	100	66,059
Dense_200	74.7	200	66,059
Dense_400	75.7	400	66,059
Medium_100	62.1	100	60,031
Medium_200	62.9	200	60,031
Medium_400	63.9	400	60,031
Loose_100	40.7	100	50,335
Loose_200	41.7	200	50,335
Loose_400	43.2	400	50,335

Table 4 Energy terms traced on rod All values at end of blow

Test ID	W_H (J)	U_R (J)	R_R (J)	$K_{R\ max}$ (J)	*ER: %*	*α */%*
Very Dense_100	178.6	10.3	-187.9	152	41.5	-0.57
Very Dense_200	171.6	-7.5	-165.4	130	42.1	0.74
Very Dense_400	177.4	-3.2	-171.4	139	43.0	-1.55
Dense_100	172.4	26.3	-206.1	164	42.9	3.57
Dense_200	177.4	3.6	-181.0	149	41.7	0.34
Dense_400	174.8	-6.7	-167.0	133	38.1	-0.67
Medium_100	179.7	36.2	-216.4	165	45.1	0.25
Medium_200	179.3	11.9	-188.3	149	40.4	-0.52

Medium_400	179.8	3.8	-182.0	155	40.0	0.21
Loose_100	182.8	90.7	-271.7	176	57.1	-0.59
Loose_200	179.9	41.4	-221.4	161	46.7	0.03
Loose_400	178.4	16.4	-194.0	149	41.5	-0.41

*maximum error in energy balance on rod divided by work done by resistance to rod

Table 5 Energy terms traced within VCC SPT system

Test ID	W_R (J)	W_{rad} (J)		W_{top} (J)		D_F (J)	D_D (J)	E_K (J)	ΔE_S (J)		α*/%
		end	*max*	*end*	*max*	*end*	*end*	*max*	*end*	*max*	
Very Dense_100	187.9	5.6	-10.9	0.5	2.9	196.0	0.22	0.45	-1.7	26.2	-0.45
Very Dense_200	165.4	20.2	-10.9	2.4	7.5	199.7	0.21	0.48	-7.9	58.1	-0.016
Very Dense_400	171.4	15.8	-10.9	5.1	20.9	210.0	0.18	0.51	-10.4	79.3	-0.39
Dense_100	206.1	-2.7	-7.4	0.1	1.1	202.3	0.75	0.63	-0.2	17.7	0.34
Dense_200	181.0	12.9	-8.9	3.7	4.9	197	0.33	0.43	-0.5	34.3	0.30
Dense_400	167.0	8.1	-12.1	2.8	13.0	179	0.26	0.43	-1.6	62.3	-0.35
Medium_100	216.4	-1.7	-5.8	0.5	1.2	212.9	0.31	0.52	0.6	7.4	0.44
Medium_200	188.3	7.3	-11.5	2.9	3.1	193.8	0.35	0.74	3.7	24.2	0.06
Medium_400	182.0	8.8	-15.8	3.6	7.4	189.3	0.43	0.62	3.4	43.4	0.58
Loose_100	271.7	0.8	-2.4	0.9	1.1	269.7	0.36	0.78	0.3	2.8	0.87
Loose_200	221.4	0.9	-4.3	0.7	1.1	220.7	0.33	0.61	0.7	4.6	0.43
Loose_400	194.0	3.1	-8.7	0.8	3.3	195.9	0.26	0.39	1.3	14.6	0.12

*error in chamber energy balance divided by rod input work

Table 6 Macroscale results of DEM-based dynamic probing tests

Test ID	q_e: *MPa*	$\Delta\rho$: *cm*	*N*	N_{60}	q_{dE} :MPa
Very Dense_100	9.96	0.67	44	31	14.17
Very Dense_200	19.89	0.36	83	58	25.56
Very Dense_400	40.03	0.24	123	87	39.16
Dense_100	6.27	1.45	21	15	6.25
Dense_200	10.30	0.7	42	30	13.77
Dense_400	29.27	0.31	97	61	28.27
Medium_100	4.71	2.27	13	10	4.63
Medium_200	11.34	1.01	30	20	9.59
Medium_400	18.80	0.5	60	40	18.99
Loose_100	1.89	5.63	5	5	2.37
Loose_200	4.04	2.54	12	9	4.29
Loose_400	9.13	0.93	32	22	10.42

Table 7 Effect of rod side friction on blow counts, resistance and end values of energy terms traced on rod

Sample	Side wall friction	*N*	*N60*	$\Delta\rho$ (cm)	q_{dE} (MPa)	W_H (J)	U_R (J)	R_R (J)	K_{R_max} (J)
Loose_200	0.52	12	9	2.54	4.29	179.9	41.4	-221.4	161
Loose_200	0	10	8	2.9	3.95	181.3	48	-230.3	171
Very dense_200	0.52	83	58	0.36	25.56	171.6	-7.5	-165.4	130
Very dense_200	0	83	50	0.36	23.92	172.3	0.19	-171.1	121

10 Figures

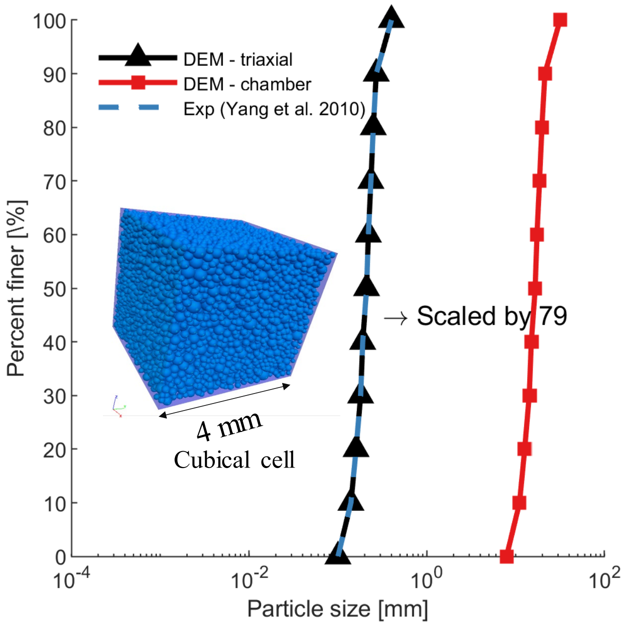

Figure 1 Particle size distribution of Fontainebleau sand and DEM models

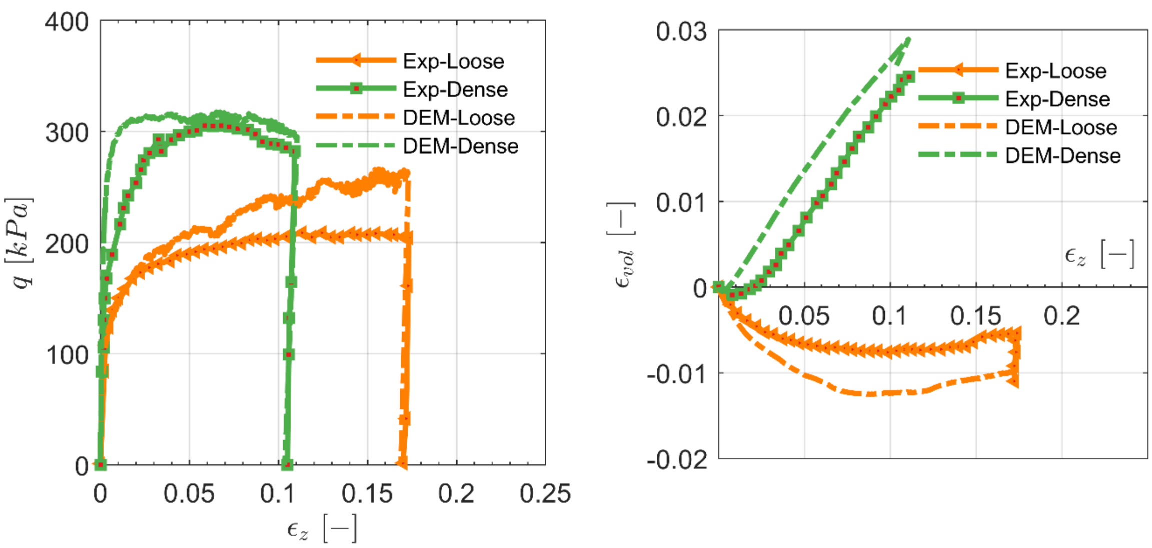

a) b)

Figure 2 Contact model calibration (G, μ, v) with triaxial tests on Fontainebleau sand from Seif El Dine et al. (2010): a) q vs ε_z, b) ε_{vol} vs ε_z. Loose means at 30% relative density; dense at 70%

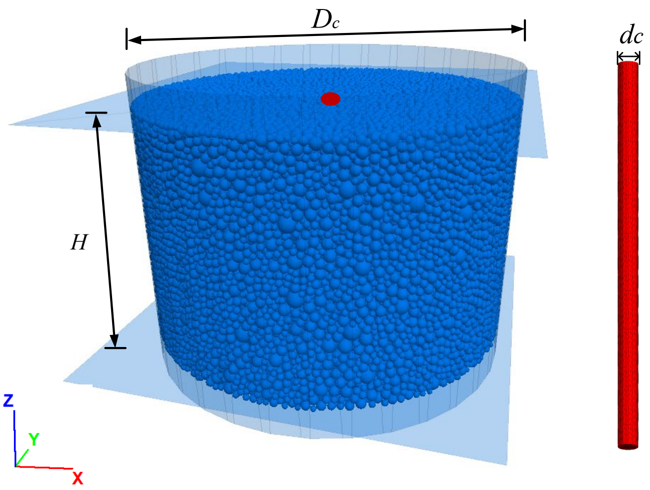

Figure 3 View of DEM model of calibration chamber, rod and coordinate (originated at the center of bottom wall

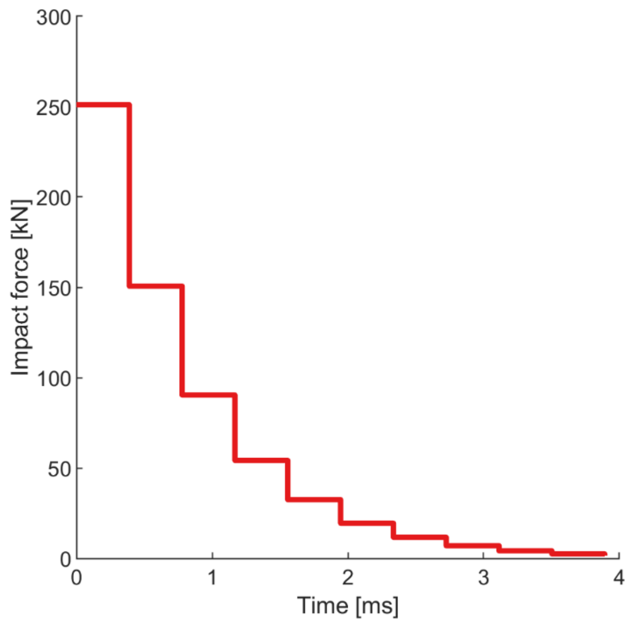

Figure 4 Input driving force F_{drv}

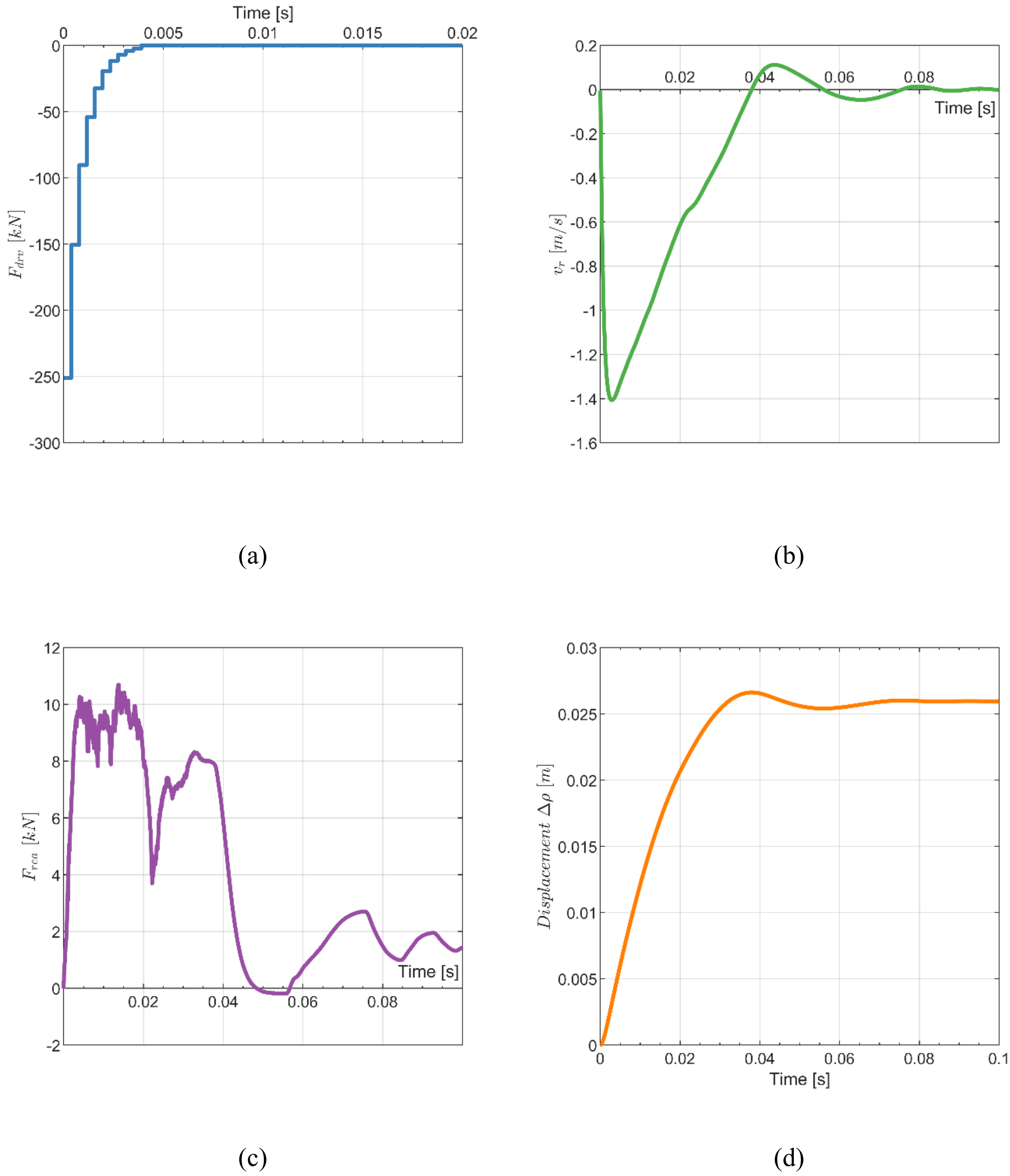

Figure 5 Example of measured variables on rod with time in an SPT (Loose_200): (a) driving force F_{drv}; (b) penetration velocity v_r; (c) reaction force on rod F_{rea} and (d) rod displacement $\Delta\rho$

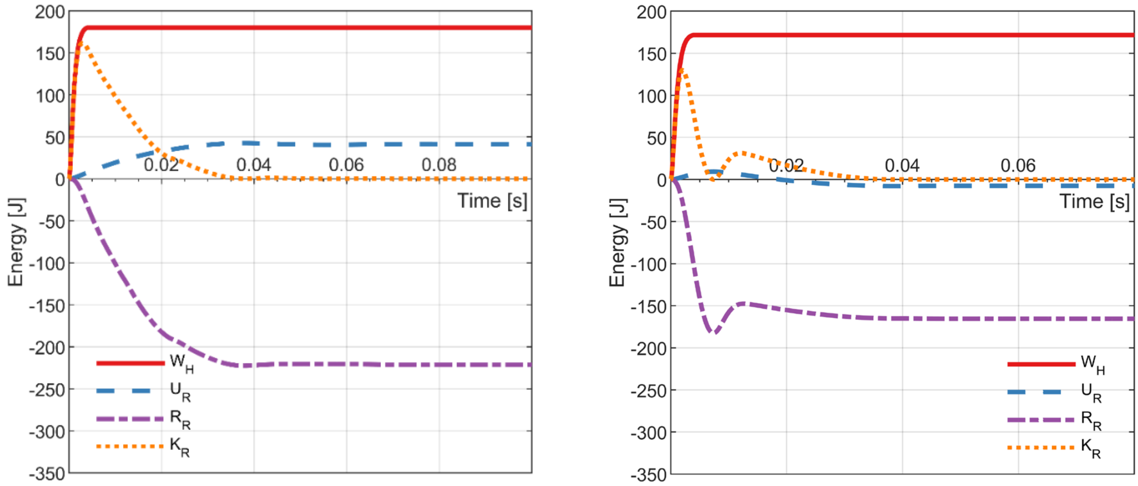

(a) (b)

Figure 6 Example energy evolution on rod (a) Loose_200 (b) Very dense_200

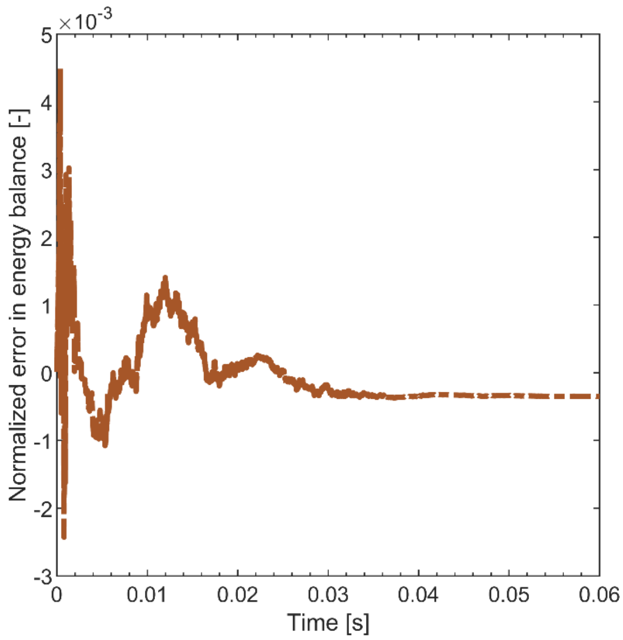

Figure 7 Error in energy balance expressed as a percentage of work done by resistance to rod (example: Loose_200)

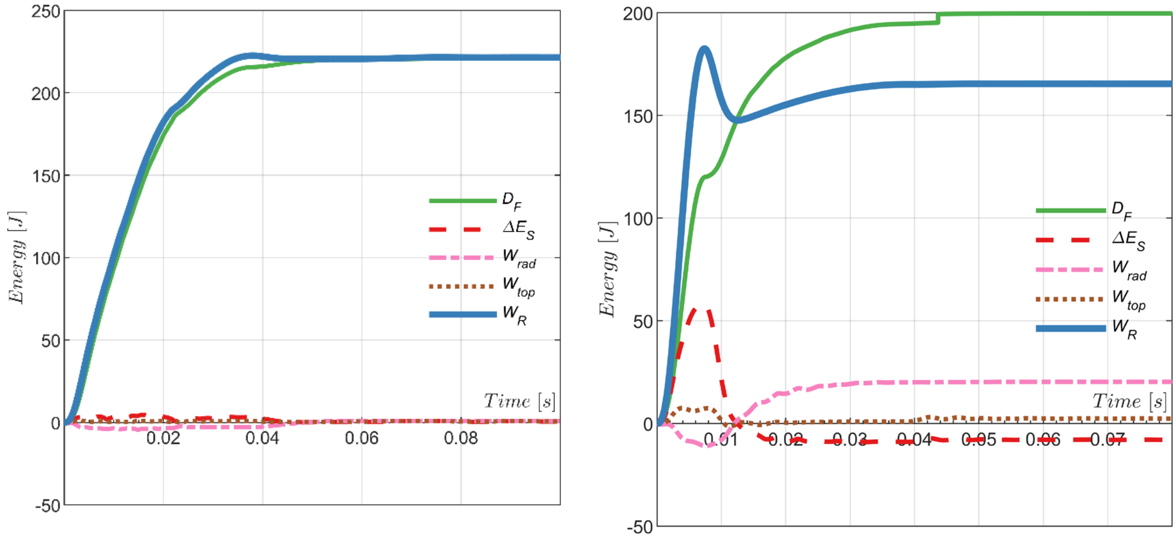

(a) (b)

Figure 8 Example energy terms evolution within VCC SPT system (a) Loose_200 (b) Very dense 200

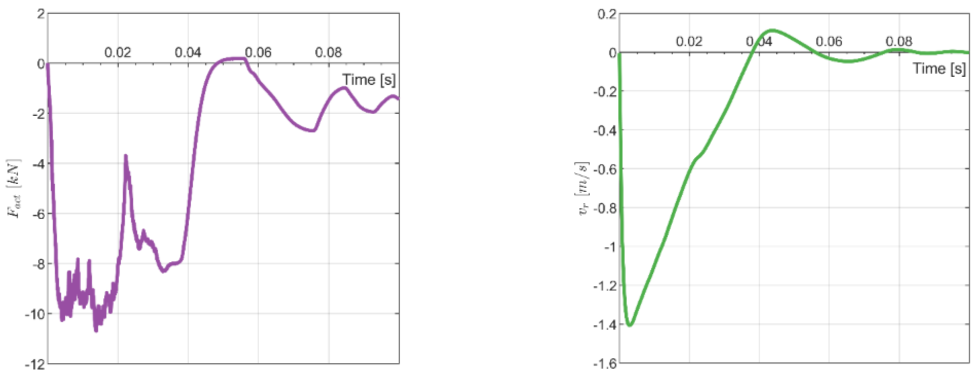

(a) (b)

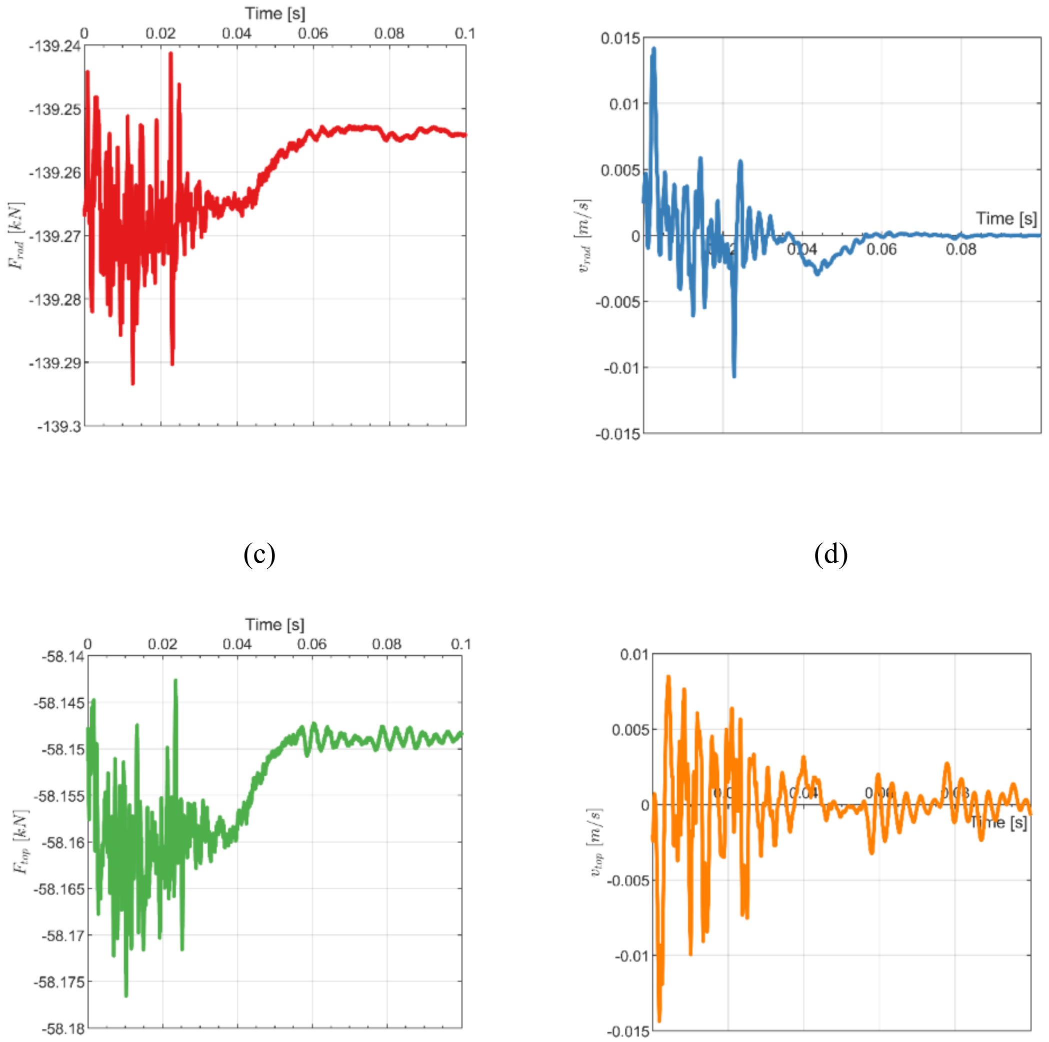

(e) (f)

Figure 9 Evolution of power conjugate variables at the chamber boundaries during an SPT blow (Loose_200): (a) rod action force F_{act}; (b) rod penetration velocity v_r; (c) radial boundary force F_{rad}; (d) radial boundary velocity v_{rad}; (e) top boundary force F_{top}; (f) top boundary velocity v_{top}

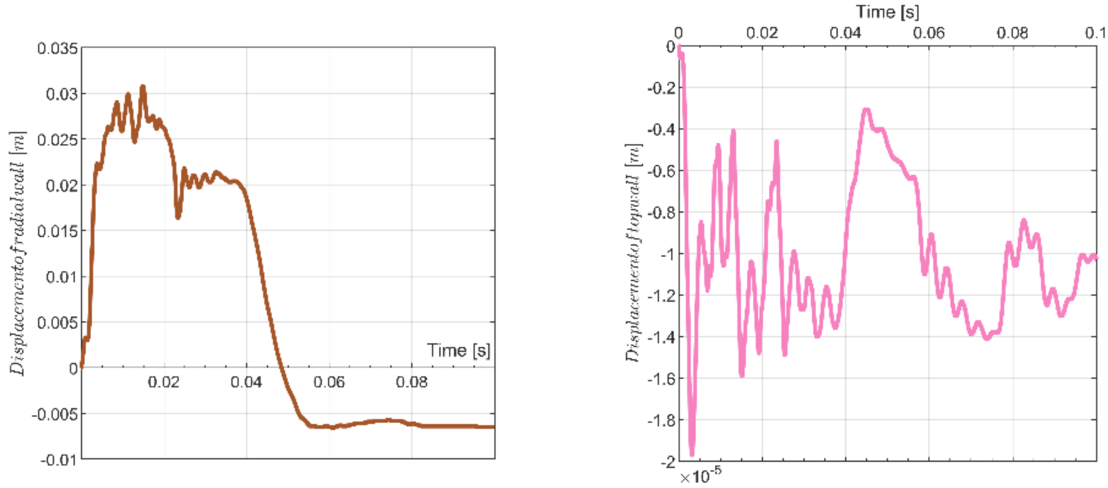

(a) (b)

Figure 10 Evolution of servo-controlled chamber wall displacements during an SPT blow (Loose_200): (a) displacement of radial wall; and (b) displacement of top wall

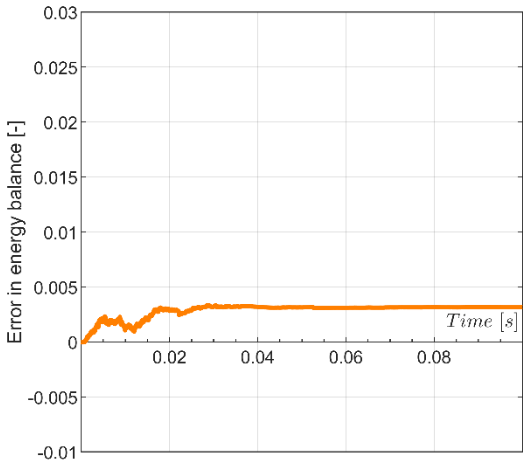

Figure 11 Error in the energy balance expressed as a ratio of rod input work (Loose_200)

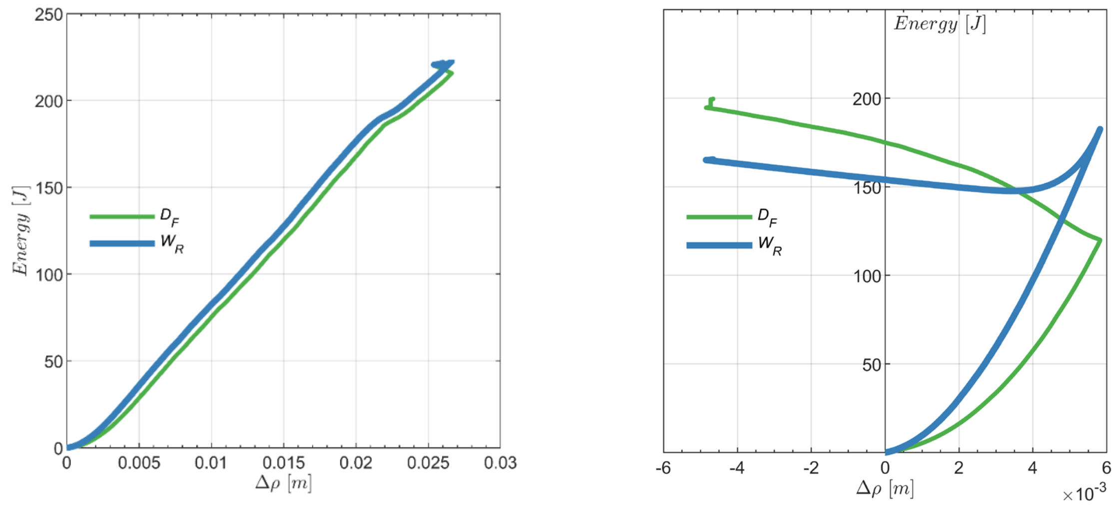

(a) (b)

Figure 12 Friction energy and rod work input vs penetration (a) Loose_200 (b) Very dense 200

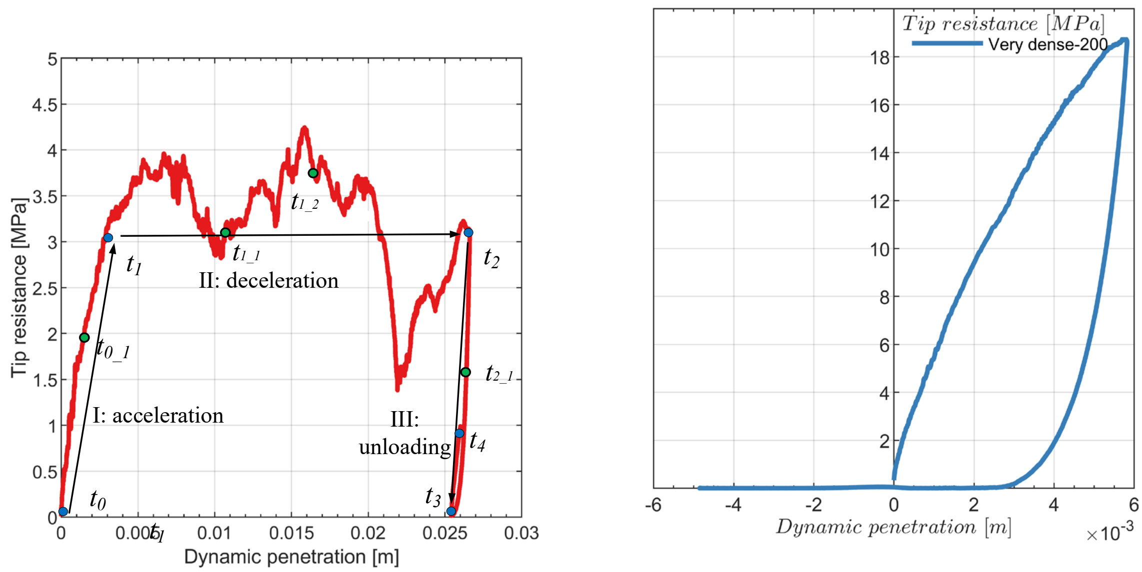

(a) (b)

Figure 13 Evolution of tip resistance with dynamic penetration (a) Loose_200 (b) Very dense_200

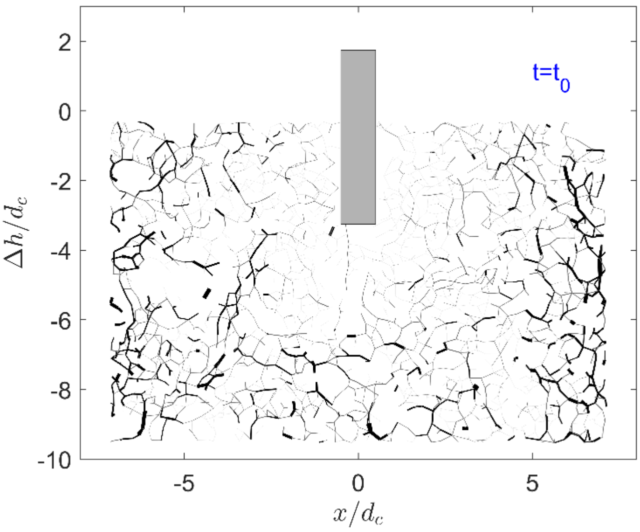

(a) t=t_0

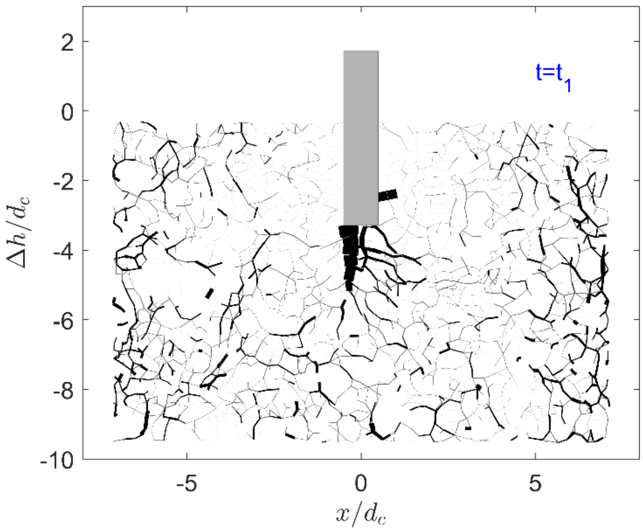

(b) t=t_1

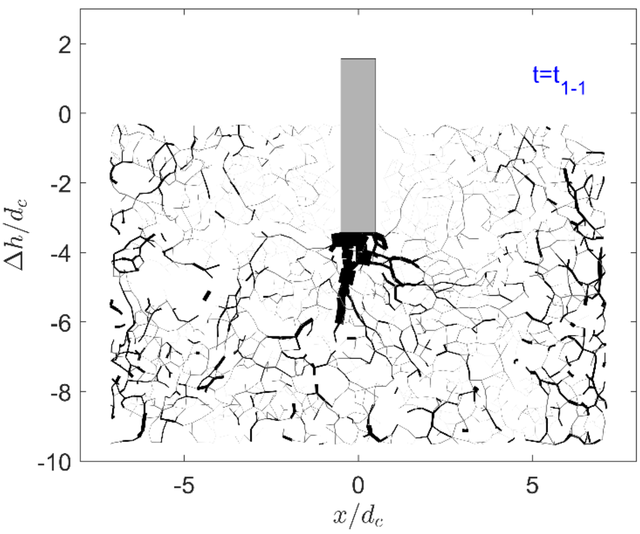

(c) t=t_{1_1}

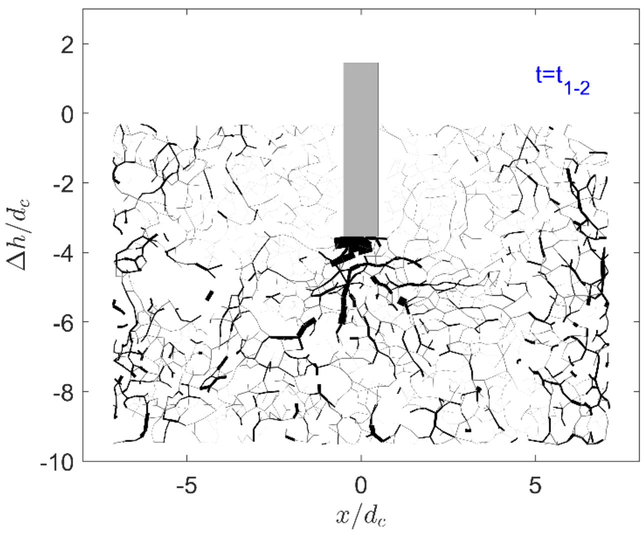

(d) t=t_{1_2}

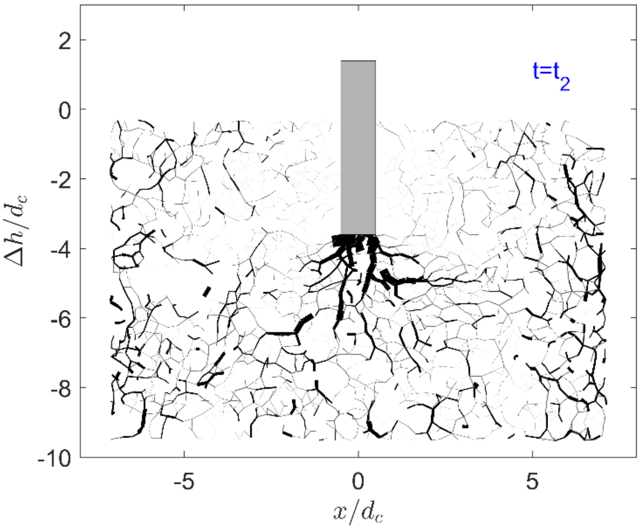

(e) t=t_2

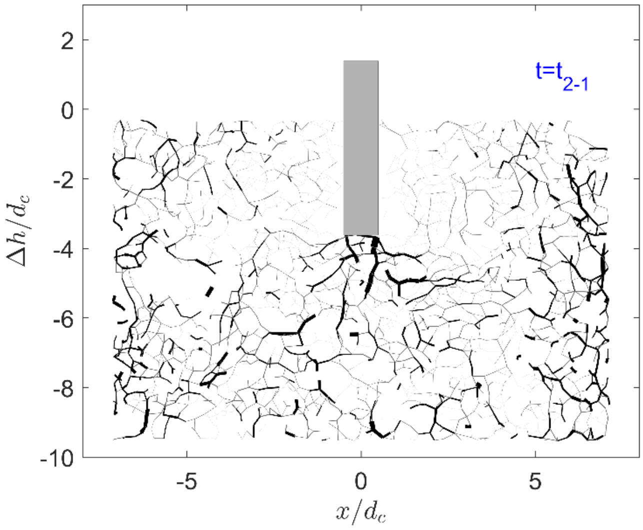

(f) t=t_{2_1}

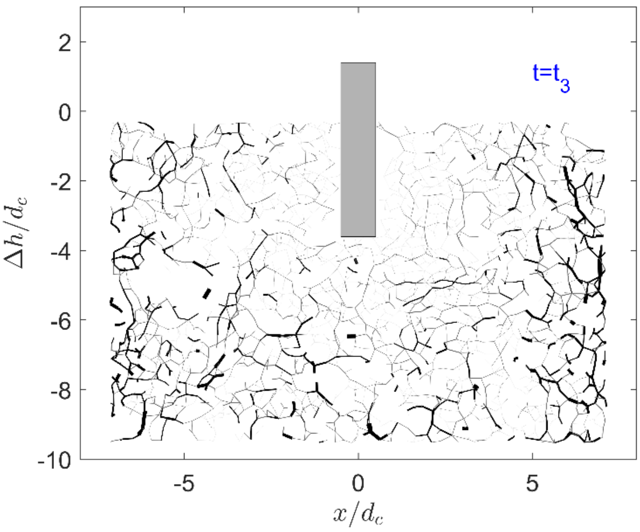

(g) t=t_3

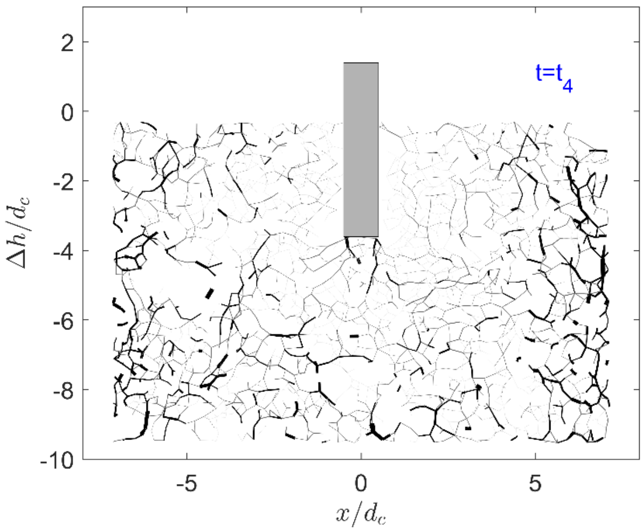

(h) t=t_4

Figure 14 Contact normal forces for particles lying within a vertical section of the chamber (test Loose_200). Forces exceeding average value +5 standard deviations are illustrated in black; large (above average but not extreme) are shown in dark gray; small (below average) marked in light gray.

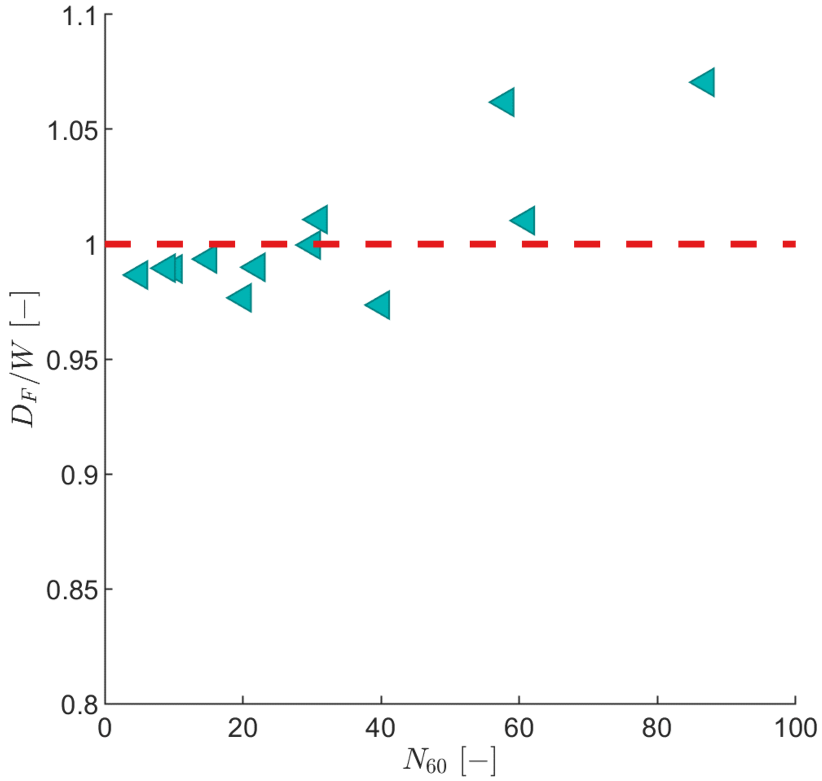

Figure 15 Energy dissipated by frictional sliding vs normalized blowcount

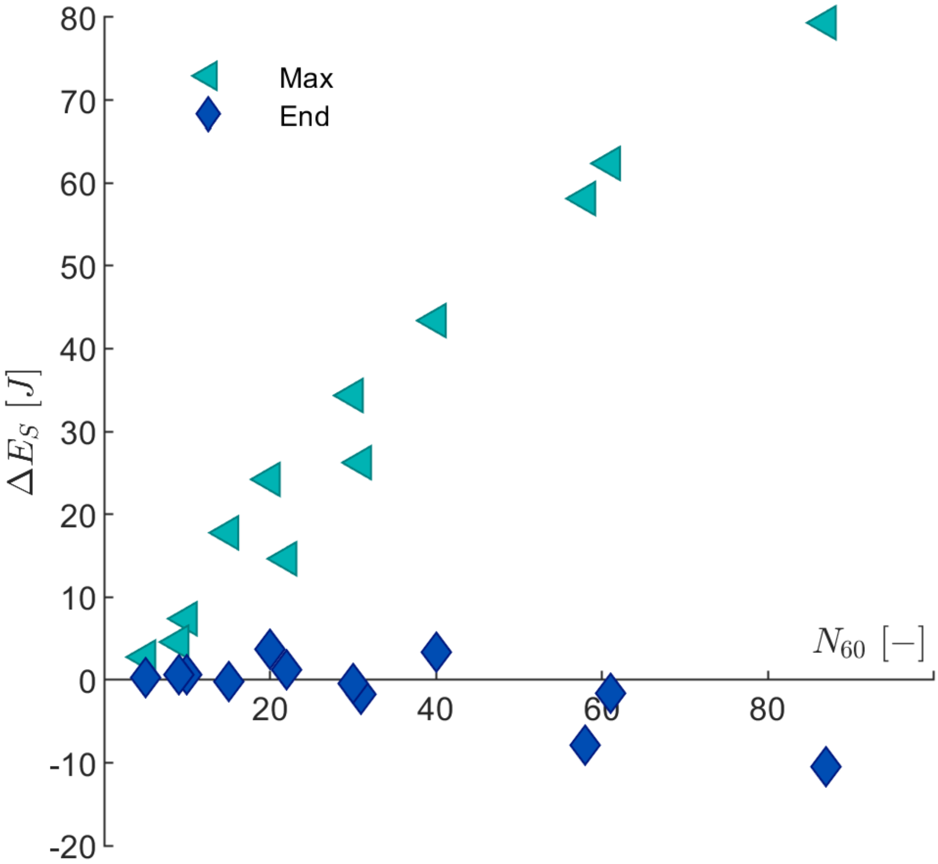

Figure 16 Maximum and end strain energy during dynamic probing vs normalized blowcount

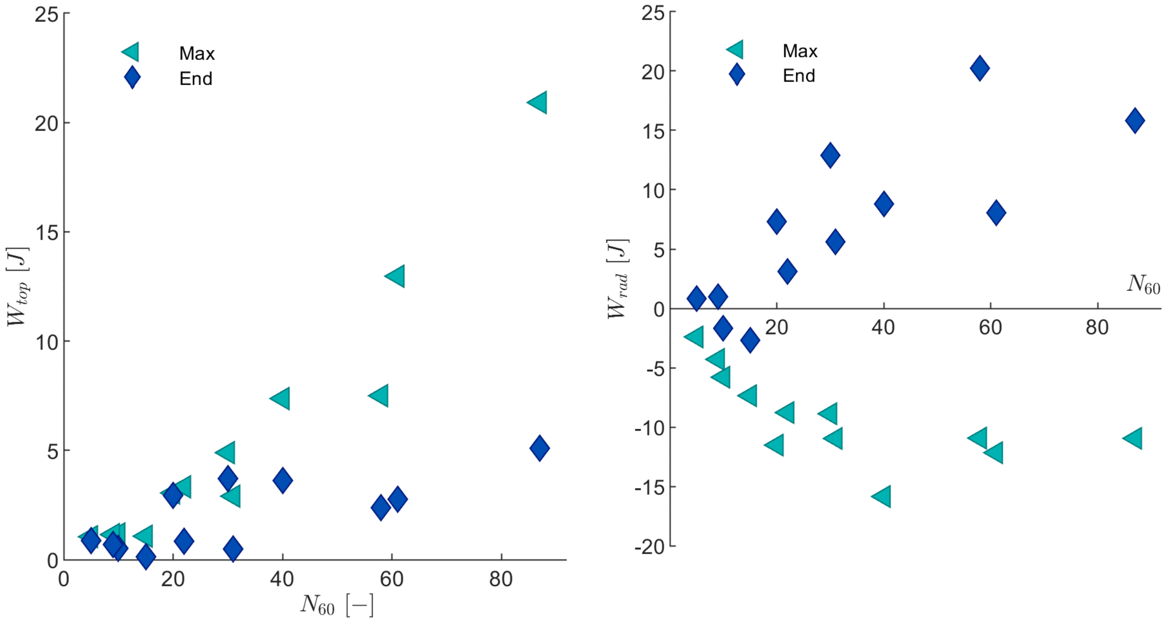

a) Top wall

b) Radial wall

Figure 17 Maximum and end work inputs vs normalized blowcount: a) top wall; b) radial wall

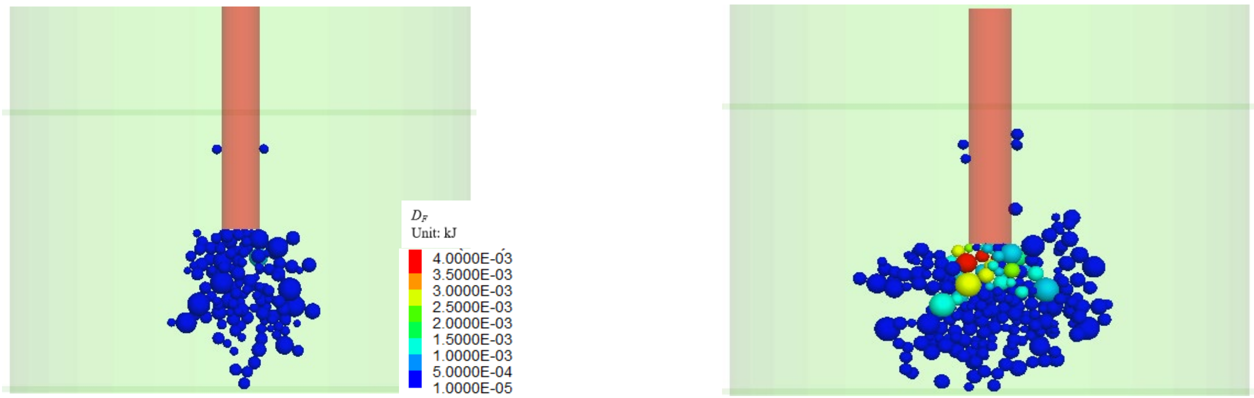

(a) $t=t_1$

(b) $t=t_2$

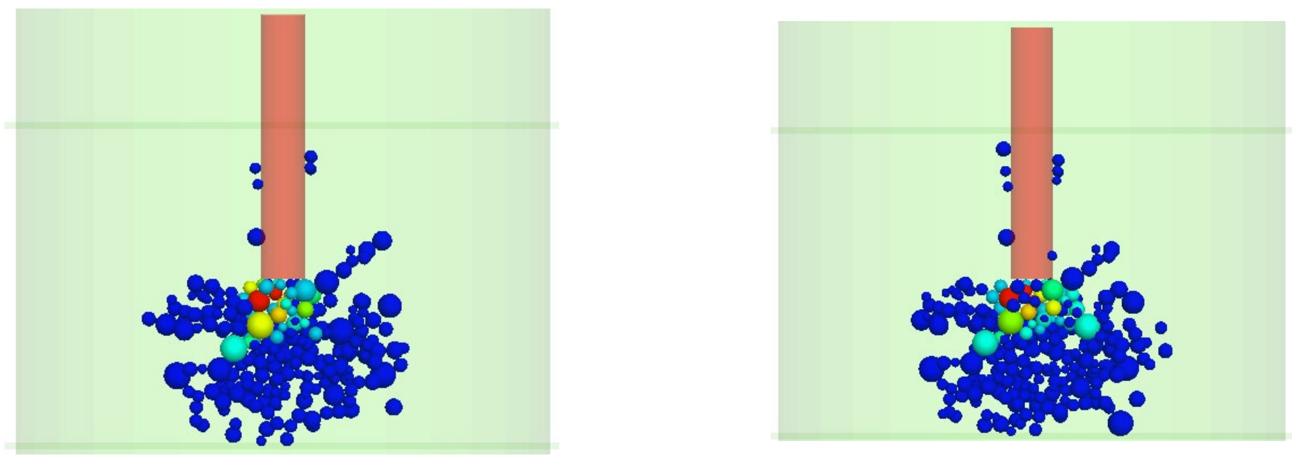

(c) $t=t_3$ (d) $t=t_4$

Figure 18 Evolution of energy dissipated by frictional sliding under impact loading (balls colored by energy dissipation)

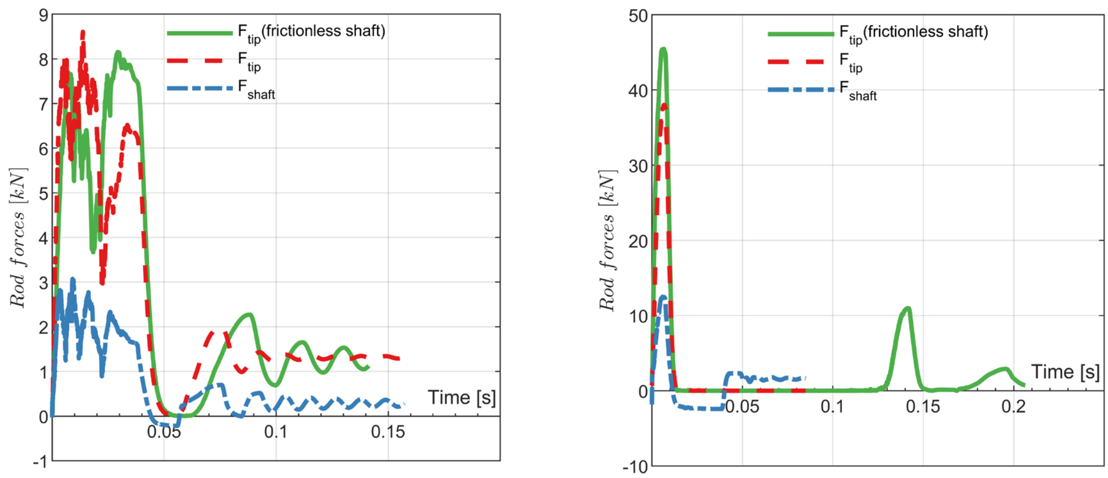

(a) (b)

Figure 19 Effect of rod side friction on the blow dynamics (a) Loose_200 (b) Very dense_200

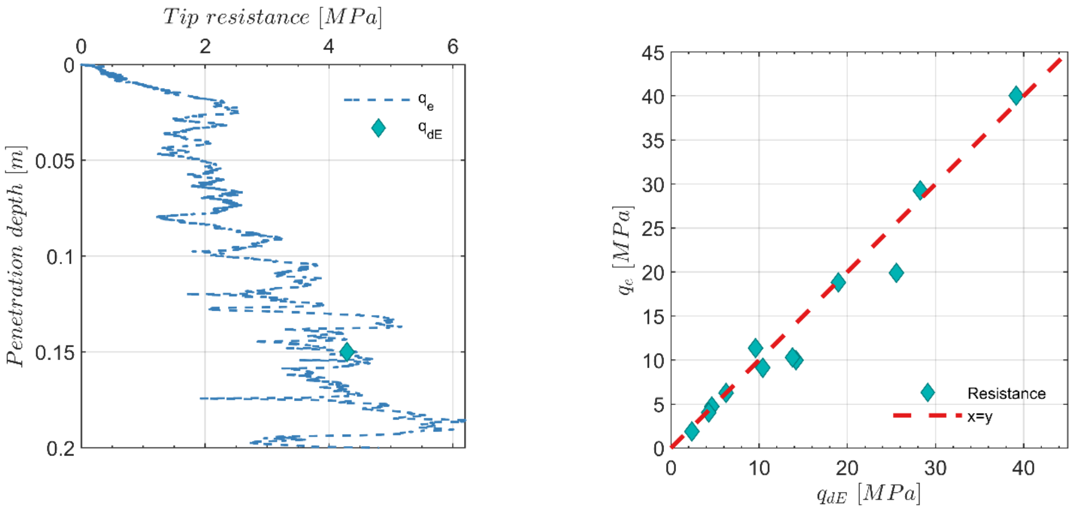

(a) (b)

Figure 20 Penetration resistance comparisons between static and dynamic tests: (a) a single case (Loose_200); (b) all cases